Article

Strain-driven Mn-reorganization in over-lithiated LiMnO epitaxial thin-film electrodes

Xiao Chen, Márton Vörös, Juan C. Garcia, Timothy T. Fister, D. Bruce Buchholz, Joseph Franklin, Yingge Du, Timothy Droubay, Zhenxing Feng, Hakim Iddir, Larry A Curtiss, Michael J. Bedzyk, and Paul Fenter

ACS Appl. Energy Mater., **Just Accepted Manuscript** • DOI: 10.1021/acsaem.8b00270 • Publication Date (Web): 23 May 2018

Strain-driven Mn-reorganization in over-lithiated $Li_xMn_2O_4$ epitaxial thin-film electrodes

Xiao Chen[1,3], Márton Vörös[2], Juan C. Garcia[1], Tim T. Fister[1], D. Bruce Buchholz[4], Joseph Franklin[6,7], Yingge Du[8], Timothy C. Droubay[8], Zhenxing Feng[9], Hakim Iddir[1], Larry Curtiss[2], Michael J. Bedzyk[3,4,5], and Paul Fenter[1*]

1. Chemical Sciences and Engineering Division, Argonne National Laboratory, Lemont, IL 60439
2. Materials Science Division, Argonne National Laboratory, Lemont, IL 60439
3. Applied Physics Program, Northwestern University, Evanston, IL 60208
4. Materials Science and Engineering Department, Northwestern University, Evanston, IL 60208
5. Physics and Astronomy Department, Northwestern University, Evanston, IL 60208
6. Energy Storage & Distributed Resources Division, Lawrence Berkeley National Laboratory, Berkeley, CA 94720
7. Electrochemical Innovation Lab, Department of Chemical Engineering, University College London, London, WC1E 7JE, UK
8. Physical and Computational Sciences Directorate, Pacific Northwest National Laboratory, Richland, WA 99352
9. School of Chemical, Biological, and Environmental Engineering, Oregon State University, Corvallis, OR 97333

*Corresponding author email: fenter@anl.gov

Abstract: Lithium manganate $Li_xMn_2O_4$ (LMO) is a lithium ion cathode that suffers from the widely observed but poorly understood phenomenon of capacity loss due to Mn dissolution during electrochemical cycling. Here, *operando* X-ray reflectivity (low- and high-angle) is used to study the structure and morphology of epitaxial LMO (111) thin film cathodes undergoing lithium insertion and extraction to understand the inter-relationships between biaxial strain and Mn-dissolution. The initially strain-relieved $LiMn_2O_4$ films generate in-plane tensile and compressive strains for delithiated ($x < 1$) and over-lithiated ($x > 1$) charge states, respectively. The results reveal reversible Li insertion into LMO with no measurable Mn-loss for $0 < x < 1$, as expected. In contrast, deeper discharge ($x > 1$) reveals Mn loss from LMO along with dramatic changes in the intensity of the (111) Bragg peak that cannot be explained by Li stoichiometry. These results reveal a partially reversible site reorganization of Mn ions within the LMO film that is not seen in bulk reactions and indicates a transition in Mn-layer stoichiometry from 3:1 to 2:2 in alternating cation planes. Density functional theory calculations confirm that compressive strains (at x=2) stabilize LMO structures with 2:2 Mn site distributions, therefore providing new insights into the role of lattice strain in the stability of LMO.

Keywords: Lithium manganese oxide, spinel, lithiation, X-ray reflectivity, strain

Introduction

Li-ion battery (LIB) technology has led a revolution in energy storage technology and continues to attract significant scientific attention[1-5]. The energy density of a LIB for a given choice of anode is defined by a combination of the lithium site density and insertion potential of the cathode. Of the various cathode materials, layered materials like $LiCoO_2$ (LCO) and lithium nickel cobalt manganese oxide (NMC) are widely used, but have multiple disadvantages including high cost and toxicity. The spinel $Li_xMn_2O_4$ (LMO)[6], has a comparable insertion potential and capacity to LCO and is attractive due to its lower cost, high natural abundance of manganese, and a more benign environmental footprint. Nevertheless, LMO has the well-known challenge of capacity loss that occurs upon repeated lithiation/delithiation cycles. This behavior is associated with the discharged LMO compositions near x=1 where LMO consists of a mixture of Mn(III) and Mn(IV). At this composition, the LMO lattice undergoes a first order transition to a tetragonally distorted phase. Beyond structural deformations due to this phase change, there is also a tendency for Mn to undergo disproportionation reactions (i.e., 2Mn(III) → Mn(II) + Mn(IV)), leading to the dissolution of Mn(II) from the LMO cathode surface[7-10]. Recent studies have demonstrated new insights into this behavior, including computational studies suggesting the face-specific differences in the presence of Mn^{3+} at the interface[11], the direct operando observation of Mn-release[12] and the demonstration of new insights into the coupled mechanical and electrochemical response of LMO electrode during lithiation/delithiation reactions[11]. However, a clear picture of the crystallographic origins of Mn dissolution at the LMO surface during operation remains largely unknown.

One challenge with respect to understanding this behavior is that lithium manganese oxides have a complex range of phases that are structurally similar and broadly distinguished by the Mn- and Li-site distributions (on the octahedral sites) within an FCC oxygen array (Figure 1). The spinel polymorph (λ-$Li_xMn_2O_4$) is cubic for $0 < x < 1$ and transforms to a tetragonal structure for $x > 1$[6, 13] (Figure 1a). The tetragonal distortion is described by a Jahn-Teller (JT) distortion of the oxygens bound to Mn(III)[6, 14] where the regular MnO_6 octahedron found at $x \leq 1$ is elongated along [001] leading to an expansion of the apical ligand bonds and a contraction of equatorial bonds (in x-y plane). In addition to the spinel phase, a number of additional LMO phases are known that are structurally related to the spinel phase (Figure 1a), including (at x = 2) the layered monoclinic phase (m-$LiMnO_2$)[15] (Figure 1b and 1c) and the orthorhombic phase (o-$LiMnO_2$)[16-18] (Figure 1d).

A second challenge to understand the Mn-loss from LMO is the need to make operando observations of the LMO–electrolyte interface so that structure-reactivity correlations can be observed directly. XR can probe the atomic-scale structure of solid-liquid interfaces including electrode-electrolyte structure as well as the adsorption and distribution of ions at charged surfaces[19-21]. To date, there have

only been a few reports in the literature of the X-ray based operando observation of a LMO (and LMNO) cathode structural developments, primarily by X-ray reflectivity (XR)[22-23], including LMO(111)- and (110)-oriented electrodes under electrochemical control during lithiation reactions[22-23]. Low angle XR measurements in the Fresnel regime of the LMO(111)-films revealed a significant (>2 nm) loss of LMO thickness and associated formation of a ~2 nm-thick surface layer upon soaking the sample in the Li electrolyte, followed by an increase in film roughness and evolution of the surface layer at potentials of 4.5 V (with respect to Li/Li^+)[22-23]. Separate measurements using the LMO thin film Bragg peaks at elevated potentials (5 V) revealed negligible changes in LMO(111) film lattice spacings that would be expected from delithiation[22-23]. But these measurements did observe significant changes to the Bragg peak intensities near 5 V that were interpreted as due to small Mn-displacements associated with a loss of symmetry, followed by substantial loss of most LMO signals at low potentials (2V)[22-23].

Here, the important role of lattice strain in controlling the phase behavior of LMO is demonstrated through *operando* x-ray reflectivity studies of epitaxial spinel $Li_xMn_2O_4$(111) films under electrochemical control for Li compositions ranging from $0 \leq x \leq 2$. These films are grown with a nominal composition of $LiMn_2O_4$ and are laterally strain-relieved with respect to the underlying $SrTiO_3$ substrate and $SrRuO_3$ current collecting film. At applied electrochemical conditions, the LMO electrodes become subject to tensile and compressive strain for $x < 1$ and $x > 1$, respectively, due to the changes to the lattice volume with lithium content. While there was little change to the LMO film morphology and structure for $x < 1$ (as expected), significant changes were observed for $x > 1$, including a reduction in the LMO film thickness and a substantial (and largely reversible) decrease in the LMO(111) Bragg peak intensity associated with the reversible site reorganization of Mn ions. This interpretation is confirmed by density functional theory (DFT) calculations that reveal an instability in the over-lithiated LMO structure (at x=2) under compressive strain leading to change in the vertical Mn site distribution from 1:3 in the spinel phase to a 2:2 ratio. This strain-driven Mn reorganization, which has not been previously reported, demonstrates the important interplay between strain and Mn-dissolution in this system.

Experimental Methods and Computational Details:

Sample Fabrication: High quality epitaxial (111)-oriented LMO films were grown on (111) $SrTiO_3$ substrates (Nikko Hitech) making use of their close lattice match[22]. The poor electrical conductivity of $LiMn_2O_4$ necessitates the use of a conductive current collector, which we implemented by incorporating a thin electrically conducting buffer layer for electrochemical control. For this, $SrRuO_3$ (SRO) was chosen as intermediate layer between $LiMn_2O_4$ and $SrTiO_3$. SRO films were coherently strained and showed excellent epitaxial lattice match with STO[24]. The LMO/SRO/STO heterostructure therefore provide the conductivity needed for electrochemical control while maintaining epitaxy. The films were grown by

pulsed laser deposition[23, 25]. The LMO target was prepared by ball milling the $LiMn_2O_4$ powder (99.9% pure, < 50 nm particle size, Sigma Aldrich) with additional 15 wt% Li_2O before uniaxially pressing into a 25 mm green-pressed pellet. The addition of Li_2O ensures near stoichiometric lithium in the deposited film due to a lower target-substrate transfer ratio for Li. The SRO target (99.9% pure, 25 mm diameter × 6.35 mm thick) was purchased from Kurt J. Lesker, USA. For film deposition, substrates were fixed to a resistive heater using silver paint and heated to 650 °C. A base pressure of $5x10^{-5}$ Torr ($6.67x10^{-3}$ Pa) was maintained and the background oxygen pressure was set at 50 mTorr (6.6 Pa). A KrF laser (248 nm) was used with 100 mJ beam energy and focused on an area of 0.05 cm^2 on the target surface (laser energy density of 2.0 $J.cm^{-2}$). Targets were held on a rotation stage at a fixed distance (50 mm) from the substrate surface. The substrates were first exposed to the plume of SRO target with 240 pulses and then switched to the LMO target with same number of pulses to give the intended nominal film thickness (~ 10 nm SRO / 10 nm LMO). After deposition, the chamber was backfilled with oxygen at 400 mTorr (53Pa) as the samples cooled.

Electrochemical Measurements and Control: The electrochemical potential of the working electrode was controlled by a CHI760D potentiostat. Li metal was used as both the counter and reference electrodes forming a half-cell, and all potentials are reported versus the Li/Li^+ redox couple. The electrolyte consisted of 1.2M $LiPF_6$ in a mixture of ethylene carbonate and ethyl methyl carbonate (EC:EMC, at a ratio of 3:7 by wt.). Cyclic voltammetry (CV) measurements were performed in two-stages, each with multiple lithiation/delithiation cycles. The first stage used a potential range between 3.5 V and 4.3 V with a scan rate of 0.2 mV/s, while the second stage scans were performed at potentials between 2.5 V and 4.3 V with a scan rate of 0.5 mV/s.

.X-ray Reflectivity Measurements: Operando X-ray Reflectivity measurements in the low angle and crystal truncation rod (CTR) regimes were performed at beamline 33BM-C of the Advanced Photon Source (APS) in Argonne National Laboratory (ANL) with an X-ray photon energy of 20.00 keV (additional measurements were performed at beamline 12 ID-D, data not shown). A specially-designed transmission electrochemistry cell [26-28] was used to study the bilayer samples as a function of applied electrochemical potential. Data were collected at fine intervals (low angle: $\Delta Q = 0.001$ $Å^{-1}$; CTR regimes: $\Delta L = 0.002$ r.l.u., corresponding to $\Delta Q = 0.0056$ $Å^{-1}$) using an X-ray area detector (Pilatus 100k).

A key result of the present study is the observation of an electrochemically induced change of the Mn site distribution within the LMO structure. Here, we outline the sensitivity of XR to these changes. The differences between the λ-$Li_2Mn_2O_4$, m-$LiMnO_2$ and o-$LiMnO_2$ structures are characterized by the Mn site distribution in the octahedral sites between the close-packed oxygen planes and can be observed by XR. The manganese ions are distributed vertically between the close-packed oxygen planes in a 3:1

ratio for λ-$Li_2Mn_2O_4$, (Figure 1a right), while the manganese ions in o-$LiMnO_2$ are equally distributed in a 2:2 ratio (Figure 1d right). In the m-$LiMnO_2$ phase, there are two ways to orient the Mn-layers, either parallel to (Figure 1b) or at an angle with the LMO (111) plane (Figure 1c), that leads to projected Mn distribution ratios of 0:4 and 2:2, respectively. These differences in the cation distributions are directly distinguished by the X-ray diffraction intensity of the LMO(111) Bragg peak at Q = 1.32 $Å^{-1}$ (for convenience, we will denote this Bragg peak using the spinel notation as LMO(111) throughout this paper). With respect to the 1:3 Mn distribution found for the λ-$Li_2Mn_2O_4$, the spinel (111) Bragg peak is absent when the Mn is distributed in a 2:2 ratio for the o-$LiMnO_2$ phase (since this reduces the repeat period of the LMO lattice by half). In contrast, the intensity for the m-$LiMnO_2$ phase will depend on the orientation of the Mn-layers. LMO (111) Bragg peak will increase in the monoclinic phase when the Mn-layers are oriented parallel to (111) with an alternating 0:4 Mn distribution ratio, while this Bragg peak intensity will vanish when orientated at an angle with the (111) plane resulting in a 2:2 distribution ratio.

Computational details: Density functional theory calculations were carried out with the plane-wave code Quantum-Espresso [29]. Electron-nuclei interactions were represented by recently developed ONCV norm-conserving pseudopotentials [30-31]. The PBE generalized gradient functional with Hubbard-U correction was used in the simplified form of Dudarev et al., as implemented in Quantum-Espresso[32]. The projectors were built using the atomic (pseudo-)wave functions and a Hubbard-U parameter of 3.5 eV was applied to Mn. We have recently used his same value to study the surface structure of spinel cubic $LiMn_2O_4$ [11]. Similar values of U were used by others to predict voltages of $Li_xMn_2O_4$ in good agreement with experiments[33-34]. A high wave function cutoff of 120 Ry was used to make the stress tensor converge. Although the ground state of $Li_xMn_2O_4$ is antiferromagnetic (AFM), we restricted our search to ferromagnetic ground states to avoid complications arising from a wide variety of possible antiferromagnetic solutions[35]. To verify that this choice did't affect our conclusion, several tests were carried out for the layered, spinel and orthorhombic $LiMnO_2$ compositions using recently reported best AFM ground states. For the monoclinic structures, we relied on previous findings that showed that the lowest energy AFM solutions require wire-like intra-layer AFM coupling of the Mn sites[36]. For the orthorhombic structure, we used the experimental AFM ordering obtained previously[37]. Here, anti-ferromagnetically coupled ferromagnetically ordered chains run through the corrugated double Mn layers which are then coupled anti-ferromagnetically in an alternating fashion. Finally, for the spinel structure we tested the best AFM arrangement found recently that was commensurate with our unit cell[35]. This was the second most energetically favorable arrangement. Although their study was carried out for the $LiMn_2O_4$ composition, we assume that the same, or similar, AFM ordering would also occur in the over-lithiated case. We used Gaussian smearing with a smearing width of 0.05 eV and 4x4x2 Gamma-centered k-mesh for the 42 atom (hexagonal) unit cell. For a few select configurations, we verified our assumption

by performing PBE+U calculations with a Hubbard-U of 5 eV on Mn and with the HSE06 functional. The HSE06 calculations were performed without relaxing the atomic positions. Structural models were built by transforming the bulk unit cells to reproduce the experimental system. The LMO spinel cubic (111) direction was chosen to be the z-direction of the unit cell. Further, a hexagonal representation of the unit cell was chosen to accommodate all of the relevant phases.

Results:

Structure of the As-Deposited $LiMn_2O_4/SrRuO_3$ Bilayer on $SrTiO_3(111)$: The as-deposited bilayer electrode structure was characterized by low angle X-ray reflectivity (XR) (Figure 2a), specular CTR data (Figure 2b) and off-specular azimuthal phi-scans to probe the film/substrate alignment (Figure 2c). Analysis of the XR results reveal the thickness, electron density and interface roughness for each layer. The derived 1D electron density profile along surface normal direction is shown in Figure 2a insert. The LMO and SRO layers have thicknesses of 102.8 ± 1.4 Å and 81.6 ± 1.1 Å respectively. Their respective XR measured electron densities of 1.14 ± 0.03 $e^-/Å^3$ and 1.77 ± 0.04 $e^-/Å^3$ match well to the bulk electron densities for LMO (1.20 $e^-/Å^3$) (measured film electron density is little bit lower due to inadequate coverage) and SRO (1.77 $e^-/Å^{-3}$). The specular CTR data (Figure 2b) include only the LMO (111) and (222) Bragg peaks which indicates a structurally homogenous film with a (111) surface orientation. Additional intensity oscillations near the LMO film Bragg peaks (often referred to as "Kiessig fringes") are due to the constructive and destructive interference of X-rays reflected from the top and bottom interfaces of the crystalline LMO film. Using the position of the film Bragg peak, the measured d-spacing of LMO(111), $d_{LMO(111)}$ is 4.75 Å, which closely matches the reported bulk d-spacing of cubic $LiMn_2O_4$(111) (4.76 Å) suggesting that the film is relaxed from the substrate's in-plane lattice. The non-specular thin-film Bragg peaks of the LMO, SRO and STO reveals that the LMO film is azimuthally aligned to the substrate lattice confirming its epitaxy and similar crystal structure. When viewed along (111) direction, cations and anions are stacked in alternating layers with 3-fold in-plane symmetry. The azimuthal orientation of the LMO{311}, LMO{400}, SRO{311} and STO{100} Bragg peaks (i.e., as a function of rotation about the surface normal direction, ϕ) are shown in Figure 2c. The observed orientations of the SRO{311} matches that from the substrate STO{100}, which indicates that SRO has the same in-plane orientation as STO. The azimuthal orientations of the LMO{311} and LMO{400} Bragg peaks shows 6 orientations, consisting of one set of three weaker peaks whose orientation matches that of STO{100} and another stronger set which is offset by 60-degrees. This indicates that the LMO film adopts two inequivalent rotational domains that each are in-plane textured and highly aligned to the substrate with the LMO (111) direction oriented along the substrate surface normal direction.

Operando Observations of LMO Structural Changes Under Electrochemical Control: The LMO/SRO/STO(111) electrode was sealed in a specially-designed X-ray transmission cell [26] in a glovebox having an Ar atmosphere, with an initial open circuit potential of 3.7 V (with respect to Li/Li^+) corroborating the nominal composition of x = 1 determined by diffraction. In the first two electrochemical cycles, the sample voltage is scanned between 3.5 V and 4.3 V at rate of 0.2 mV/s corresponding to Li stoichiometries ranging between $0 < x < 1$. (Periodic gaps in the plotted CV current are associated with spikes in the current that are induced by the incident X-ray beam and have been removed for clarity. These spikes are associated with photoelectron production and do not influence the lithium intercalation). Cyclic voltammetry data (Figure 3a) clearly show two redox couples at 4.0 V and 4.16 V with little polarization, matching the known electrochemical response of bulk LMO powders[38]. CVs at successive cycles nearly overlap, indicating good capacity retention in this voltage region. In the second stage of cycling (3rd through 5th cycles), the discharge voltage was lowered to 2.5 V and the scan rate was increased to 0.5 mV/s with an additional redox couple appearing below 3 V (Figure 3b) for lithium composition ranging between $1 < x < 2$. In this stage, the redox features exhibit higher polarization and broadening, and generally diminish with each cycle indicating capacity loss. These results are fully consistent with the known bulk LMO electrochemical behavior[6] associated with the Mn redox from Mn(IV) at x=0, a mixture of Mn(IV) and Mn(III) at x=1, and Mn(III) at x=2.

Repeated CTR measurements near the LMO (111) Bragg peak started in the middle of 2nd cycle (3.5V). The 2D color map in Figure 3c provides an overview of the changes to the LMO (111) Bragg peak changes with respect to the applied potential. These results show that the LMO Bragg peak exhibits significant changes in position, width and intensity as a function of applied potential, indicating that the film structure and morphology evolved during lithiation/delithiation reactions. These changes are quantified by fitting the LMO(111) Bragg peak with a Gaussian function and a linear background, revealing the peak position (Q_{111}), the peak width (ΔQ_{111}), and the integrated intensity (I) versus time (as indicated in Figures S1, S2). These parameters reveal the LMO(111) d-spacing and the crystalline LMO film thickness (through the Scherrer equation $t = 2\pi/\Delta Q$). The integrated peak intensity is sensitive to multiple factors including the film coverage and the internal LMO crystal structure (*e.g.*, the Mn-site distribution).

The evolution of these parameters is plotted along with the applied potential as a function of time (Figure 4). These results are discussed within four different time regimes, corresponding to the following changes in applied potential and lithium stoichiometry: ① a discharge/charge cycle from 4.3 V to 3.5 V and back to 4.3 V (*i.e.* x = 0 to 1, and then to 0); ② discharge from 4.3 V to 3 V (*i.e.* x = 0 to 1); ③ deep

discharge from 3 V to 2.5 V and back to 3 V (*i.e.* x = 1 to 2 and then to 1); and ④ charge from 3 V and to 4.3 V (*i.e.* x = 1 to 0).

The LMO lattice spacing (Figure 4b) is a direct indication of the lithiation state as Li insertion into LMO increases its lattice volume. The measured LMO d-spacing at 3 characteristic compositions (nominally x = 0, 1, and 2) is noted as $d_0(Mn_2O_4)$, $d_1(LiMn_2O_4)$ and $d_2(Li_2Mn_2O_4)$, which are compared to the corresponding d-spacing values of bulk LMO (D_0, D_1 and D_2 respectively). The observed values of d_0 and d_1 are close to D_0 and D_1 (within 0.8%), but d_2 is significantly larger than D_2 (by 3.5%). The LMO d-spacing ratio in $d_2/d_1 = 1.042$, is close to the expected volume change in bulk LMO between $Li_2Mn_2O_4$ to $LiMn_2O_4$ ($V_2/V_1 = 1.054$). This suggests that, as expected, the LMO epitaxial thin film is laterally pinned to the substrate and compressive in-plane strains are present for lithium compositions of x >1.

The changes of effective LMO film thickness (Figure 4c) with respect to applied voltage provide additional insight into the LMO reactivity. The thickness is stable when cycled above 3 V as shown (regions ① and ②) with a measured thickness of 105 $\pm$ 2 Å, consistent with the *ex situ* XRR characterization result (102.8 Å). However, there is a significant and irreversible decrease of the measured film thickness when LMO film is discharged below 3 V (region ③). Such behavior can be due to multiple causes, including a reduction in the crystalline thickness of the electrode (either due to simple dissolution, or to the formation of a surface reconstruction that is structurally-distinct from the tetragonal phase), or potentially due to an inhomogeneous vertical strain distribution within the film (e.g., due to a vertical Li compositional gradient). Of these mechanisms, only the first leads to a reduction in the physical film thickness. In order to distinguish these mechanisms, we also performed additional low-angle XR measurements that directly probed the LMO film thickness that compared the operando film structure initially and after 5 charge discharge cycles (Figure S3). These results directly reveal a reduction of LMO thickness (from 102.8 Å to 90.5 Å) and an increase in the LMO surface roughness (from 5.0 Å to 14.9 Å). These results are only consistent with the reduction in the LMO film thickness, and is fully consistent with reported capacity fading in this region, which is due to loss of active material through Mn dissolution. These results, along with the variation in the LMO lattice spacing, are consistent with known lithiation behavior of LMO (except for the evidence for compressive strain in the fully lithiated phase).

Additional insights into the changes to the film structure are revealed in the evolution of the integrated intensity of LMO (111) Bragg peak (Figure 4d). The intensity is nearly unchanged when cycled beyond 3V (regions ① and ②). However, an 80% decrease is observed for applied voltages below 3 V (region ③, the onset potential for lithiation to x=2). This change is partially recovered upon delithiation above 3 V (region ④ for x < 1) (and may have fully recovered if it were held for a longer period of time

at elevated potentials). This 80% intensity drop is surprising, as the electron density of the LMO does not change significantly with the insertion of Li. Nor can it be attributed to a loss of the LMO film since the LMO thickness is reduced by only 10% in this region ③ and we observe that this intensity is partially recovered at higher applied potentials. This suggests that the loss of intensity is due to a reversible restructuring of the LMO film. Subsequent scans reveal similar behavior. This includes largely reversible changes in lattice spacing and modest irreversible reductions in the LMO film thickness for each cycle at potentials below 3 V. The data also show a continued damped oscillatory loss of the LMO(111) Bragg peak intensity when the potential is driven below ~3 V in each lithiation cycle. This suggests that this transformation is a kinetically slow process, consistent with the large polarization observed in the CV data near the 3 V (Figure 3). Together these results indicate that the behavior seen in the first cycle was representative of the response of the epitaxial LMO electrode.

Additional CTR measurements were performed on an equivalent, separately prepared, electrode to understand the apparent loss of LMO(111) intensity by comparing the XR signal for the as-deposited film with that after 10 lithiation/delithiation cycles (Figure 5). Here, an electrode consisting of 10 nm LMO / 30 nm SRO / STO (111) was cycled between 2.5 V and 4.3 V at a rate of 0.5 mV/s. These results reveal that the while the as-deposited film has well-defined LMO (111) and (222) Bragg peaks, after cycling the LMO(111) Bragg peak is strongly attenuated while the LMO (222) Bragg peak remains with only modest changes in position and intensity. This is direct evidence that the loss of LMO(111) Bragg peak intensity is not due to a loss of LMO film crystallinity or coverage and that the oxygen-framework of the LMO film is preserved through these electrochemical cycles (except for the reduction in LMO film thickness). This result is consistent with the oscillatory decay in the LMO(111) Bragg peak intensity observed in the operando measurements (Fig. 4d).

This large decrease in the LMO(111) intensity without significant changes in the LMO(222) reflection is explained by changes in the internal structure of the LMO film for $x > 1$. The intensity of the LMO(111) Bragg peak derives from the modulation of the Mn ion occupation in alternating layers with a 1:3 ratio. A simple explanation for the observed loss of intensity is that the Mn site distribution changed to a 2:2 ratio due to the migration of Mn ions from the Mn-rich layer to the Mn-poor layer. For such a structure, the LMO (111) Bragg peak diffraction becomes forbidden (*i.e.* zero in intensity) while LMO (222) is largely unaffected. Based on the XR results, we conclude that the loss of LMO(111) Bragg peak intensity on subsequently deep lithiation cycles ($x>1$) is associated with a thermodynamically-driven, but kinetically-limited, reorganization of the Mn ions within the LMO host lattice.

The close structural relationships between various LMO structures shown in Figure 1[39] suggest that this is at least conceptually feasible as it only requires a cation reorganization while maintaining the

oxygen sublattice. Nevertheless, the ability to transform between these structures requires Mn site-exchange between the octahedral sites. For example, a transformation from the λ-$Li_2Mn_2O_4$ to either the o-$LiMnO_2$ or m-$LiMnO_2$ requires 1/4 of manganese ions to migrate across the oxygen stacking planes[40-42]. This is expected to be a kinetically-hindered process, consistent with the experimental observations.

Additional insights into the possible changes of $Li_xMn_2O_4$ film as a function of strain and lithiation level were obtained by density functional theory (DFT) calculations. The question that these calculations were designed to answer was whether the presence of lateral compressive strains in the epitaxial film for compositions of $1<x<2$ could change the relative stability of the different LMO phases, as suggested by the XR data. Since it is known that the tetragonal phase for <1 is the most stable phase for unstrained LMO, the unexpected loss of the LMO(111) Bragg peak intensity occurs at the second lithiation plateau at 3 V, we concentrate on the relative stability of the over-lithiated phase with composition $Li_2Mn_2O_4$ to explore if there is an energetic driving force for structural changes. In order to be consistent with the experimental conditions, the DFT calculation adopted a hexagonal unit cell with a fixed in-plane lattice spacings, a = b, and the angle between these directions, $\gamma = 120°$. To address these questions, we calculate the relative energy per formula unit for the fully lithiated $Li_2Mn_2O_4$ as a function of the in-plane lattice constant (Figure 6) for the four structures shown in Figure 1 taking the tetragonal phase as a reference and allowing the vertical LMO layer spacing to relax for each value of in-plane strain. For x=2 and in the absence of lateral strain, the tetragonal phase has ground state energies that are similar to that of the monoclinic phase I and orthorhombic phases with energy differences within a few tens of meV per formula unit, but it is not the energetically most favorable structure, in agreement with prior theoretical calculations[43]. Note that the results in Figure 6 is specific to $Li_2Mn_2O_4$ and does not address the relative stability of these phases at other Li stoichiometries.

Due to the epitaxial constraint on the LMO film and the known differences in the bulk spinel LMO structure as a function of Li content, we estimate that the films will be under a ~4% compressive strain when fully lithiated. The DFT results show that incorporation of compressive in-plane strain changes the relative stability of these phases. The monoclinic phase I (Figure 1b) is energetically highly unfavorable with compressive in-plain strain. However, the monoclinic phase II (Figure 1c) develops a cooperative Jahn-Teller distortion that leads to a decreased energy. The JT distortion is cooperative since every Mn-O octahedron distorts in the same manner. In the cooperative JT phase, the fcc oxygen lattice became corrugated in the plane parallel to the substrate to accommodate the elongation of the Mn-O octahedrons perpendicular to the substrate. The energetic stabilization of the monoclinic phase II can also be attributed to its ability to accommodate compressive strains since it has a strongly anisotropic elastic response. Indeed, the monoclinic phase II is "softer" in the direction of the applied strain since it has more

Li-O bonds whereas the monoclinic phase I only has the "harder" Mn-O bonds within the Mn-O plane in the direction of the strain. Moreover, the orthorhombic phase (Figure 1d) is also more stable than the tetragonal phase under compressive in-plain strain. These results reveal that both the monoclinic II and orthorhombic phases of the fully lithiated $Li_2Mn_2O_4$ have lower energies than the tetragonal phase under our experimental condition, and both have the Mn-site distribution that leads to the loss of the LMO(111) Bragg peak. From these differences in stability and the apparent reversibility of the LMO(111) intensity loss upon delithiation, we conclude that the observed changes in the Mn distribution from that found for the spinel phase (1:3) (for $x < 1$) to the observed 2:2 ratio (for $1<x<2$) are thermodynamically-driven for these epitaxial thin-film LMO cathodes. That is, our results reveal that the over-lithiated LMO structure is susceptible to an internal redistribution of the Mn site distribution under compressive in-plane strain (imposed by epitaxial constraint of the thin-film). Through the combination of experimental observations and theoretical calculations, we conclude that applied strain enables the local redistribution of the Mn ions distribution (presumably through oxygen layers) leading to a change of Mn distribution ratio in alternating cation layers from the 1:3 value in the tetragonal phase to a 2:2 distribution that is equally distributed.

Discussion:

These results can be compared and contrasted with other results concerning the aging of cathode materials where structural phase transitions are seen as an important cause for the cathode degradation[44-45]. In this respect, the visible reduction of LMO film thickness observed at the onset of the ~3 V lithiation plateau (*i.e.* for $x>1$) is fully consistent with the onset of the Jahn-Teller distortion associated with the transition from cubic to tetragonal spinel and the associated disproportionation reaction of Mn leading to dissolution of Mn^{2+}. In this respect, the model films used here reproduce the widely observed capacity loss behavior of LMO. A secondary impact of this phase transition and the associated volume/shape change of the LMO is the internal stresses that might accumulate in a dense cathode. Recent results from Çapraz et al.[46] demonstrated the strong correlation between lithiation reactions and the development of internal stress, as well as the more subtle but important asynchronous development of stress and strain. Recent studies have even mapped strain distributions within a given spinel cathode particle[47-48]. While these relationships were observed on the 4.1 V plateau where Mn-loss is less significant than on the 3 V LMO plateau, recent operando studies have demonstrated that Mn-loss also occurs on the 4.1 V plateau.[49]

The present study has added an additional level of understanding in showing that externally applied stress (*i.e.* in our case, through the epitaxial constraint of the thin-film cathode) can significantly alter the phase behavior of the LMO cathode upon lithium insertion. Remarkably, strain-driven re-organization occurs throughout the thin-film cathode. In this sense, the transition that we observe is no

longer a simple insertion reaction but instead involves a more subtle topotactic reaction in which the cation site distribution in LMO is altered upon insertion of the second Li ion (while preserving the O-sublattice). Such Mn-migration is normally associated with an irreversible change in the structure, typically to an inert rock-salt phase. Furthermore, the motion of the Mn across the densely packed oxygen planes is facilitated by the migration of Mn from the octahedral (16d) sites to the tetrahedral sites that is coupled to the transformation to Mn^{2+} via a disproportionation reaction and the known higher solubility of Mn^{2+} in the electrolyte[50-51]. In this sense, it is apparent that the loss of Mn at the surface of the cathode is intimately connected with both the stress development of Jahn Teller distortion (that drives the Mn-site migration) and tendency of Mn to undergo a disproportionation reaction. This behavior may be increasingly important for LIB cathodes when using ultrathin graphene binders[52] where the direct contact between individual grains and the volume changes from lithiation may lead to significant stresses.

Conclusions:

These studies reveal new insights into the role of strain in altering the structure and electrochemical reactivity of insertion $LiMn_2O_4$ cathodes. The use of single-phase epitaxially-constrained (111) LMO thin films exhibits reversible lithiation reactions. The results, obtained through operando observations, reveal the coupled strain evolution (by measurements of the vertical lattice spacing), Mn-loss (by reduction of film thickness), and cation migration (through the loss of the LMO(111) Bragg peak intensity as a function of lithium content). While a simple insertion reaction are observed for $0<x<1$, the epitaxially constrained spinel LMO undergoes a topotactic reaction for $x>1$ that is characterized by a Mn-site redistribution that preserved the O-sublattice structure. Density functional theory calculations confirm that compressive strains (at $x=2$) stabilize LMO structures with 2:2 Mn site distributions. The appearance of this structural transformation is correlated with the onset of Mn-loss, suggesting that the mobility of the Mn within the LMO lattice appears to be correlated to the loss of Mn from the surface due to reaction with the electrolyte. A key observation in the present results is that the change in Mn site distributions is observed to be reversible. This is distinct from the known instability of the orthorhombic phase to transform irreversibly into the spinel structure upon electrochemical cycling. These results provide useful benchmark for understanding the well-known voltage fade in lithium- and manganese-rich layered composite oxides. In particular, the present results reveal that the "layered to spinel" structural modification/rearrangement, which is seen as a major reason for this voltage fade[53], can be reversible under compressive strains. More broadly, these results provide new and direct insights into the role that the metastability of lithium manganese oxides plays in the context of lattice strain and provide a new basis for understanding approaches to control the secondary reactivity of insertion cathodes, in particular widely observed Mn-loss in LMO.

Acknowledgements:

This research was primarily supported by the Center for Electrochemical Energy Science, an Energy Frontier Research Center funded by the U.S. Department of Energy, Office of Basic Energy Sciences through Argonne National Laboratory. Argonne is a U.S. Department of Energy laboratory managed by UChicago Argonne, LLC, under contract DE-AC02-06CH11357. Research at the Advanced Photon Source (Station 33BM-C, 12ID-D) at Argonne National Laboratory was also supported by DOE. Computer time allocations at the Argonne's Laboratory Computing Resource Center, and the National Energy Research Scientific Computing Center (NERSC, supported by the Office of Science of the U.S. Department of Energy under Contract no. DE-AC02-05CH11231) are gratefully acknowledged. M.V. was supported by the Director, Office of Science, of the U.S. Department of Energy under Contract No. DE-AC02-06CH11357 (Argonne Research Scholar). D.B.B acknowledges the Pulsed Laser Deposition Shared Facility at the Materials Research Center at Northwestern University that is supported, in part, by the CEES-EFRC program, as well as by the National Science Foundation MRSEC program (DMR-1720139) and the Soft and Hybrid Nanotechnology Experimental (SHyNE) Resource (NSF ECCS-1542205). One sample in these studies was made by Y.D., who is funded by the DOE Early Career Research Program for the support on thin film growth performed at the W. R. Wiley Environmental Molecular Sciences Laboratory, a DOE User Facility sponsored by the Office of Biological and Environmental Research. J.F. acknowledges support from the European Union Horizon 2020 under the Marie Sklodowska-Curie grant agreement No. 705339 and is grateful for support from the Science and Technology Facilities Council Early Career award, ST/K00171X/1. Dr. Javier Bareño is acknowledged for helpful discussions.

Supporting Information. Additional information includes an explanation of the fitting procedure of the LMO Bragg peak shape and position (Figure S1), fits of the LMO Bragg at representative lithiation states (Figure S2) and fits to the low-angel X-ray reflectivity data in the Fresnel regime before and after cycling with the associated fitting parameters (Figure S3).

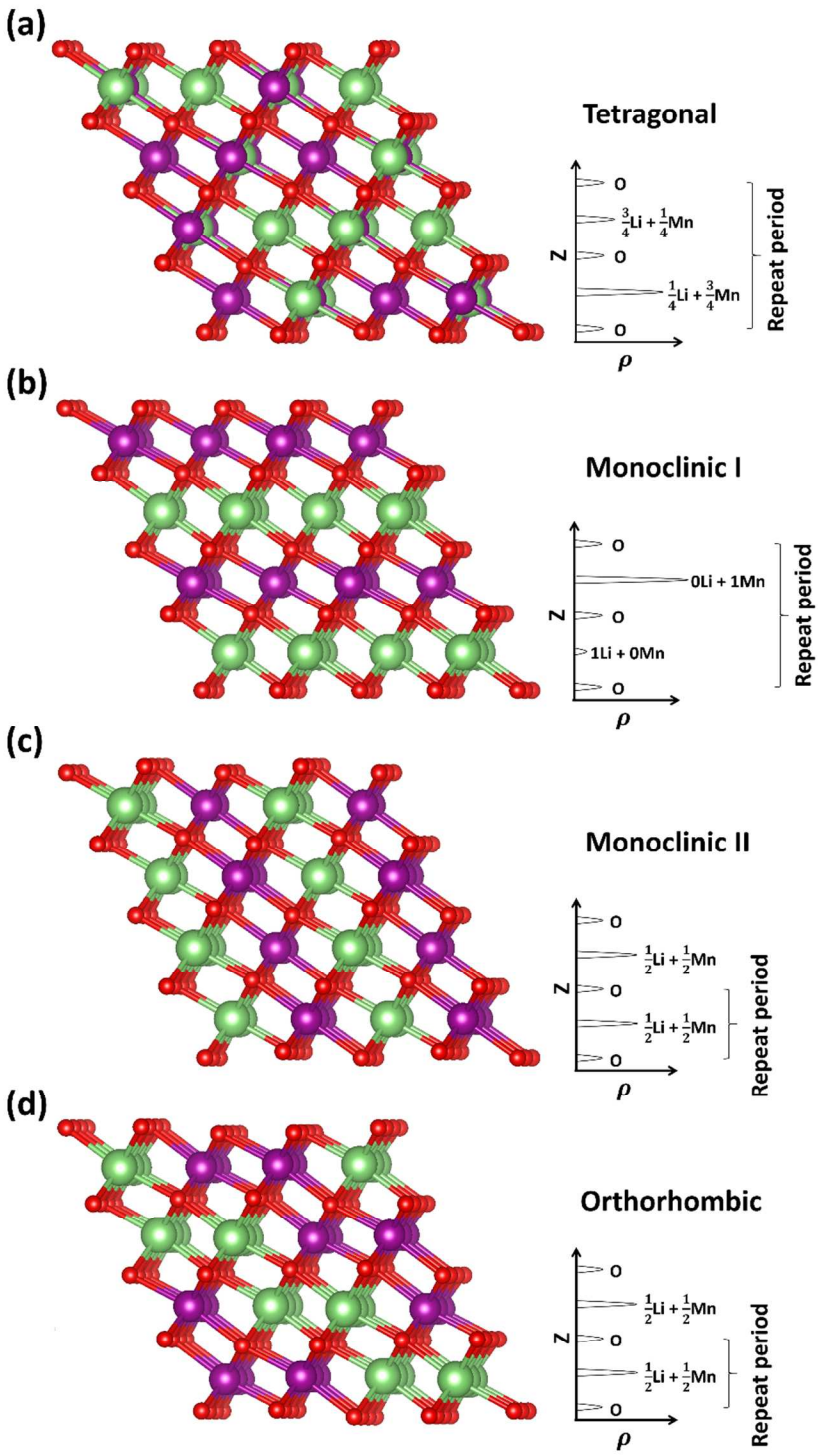

Figure 1: Crystal structure (side view of close-packed oxygen arrays) for (a) tetragonal λ-$Li_2Mn_2O_4$; (b)(c) monoclinic m-$LiMnO_2$ with 2 different stacking orientations and (d) orthorhombic o-$LiMnO_2$. Red, purple and green balls represent oxygen, manganese and lithium atoms, respectively. Projected electron density profiles along [111] direction for each structure are depicted on the right.

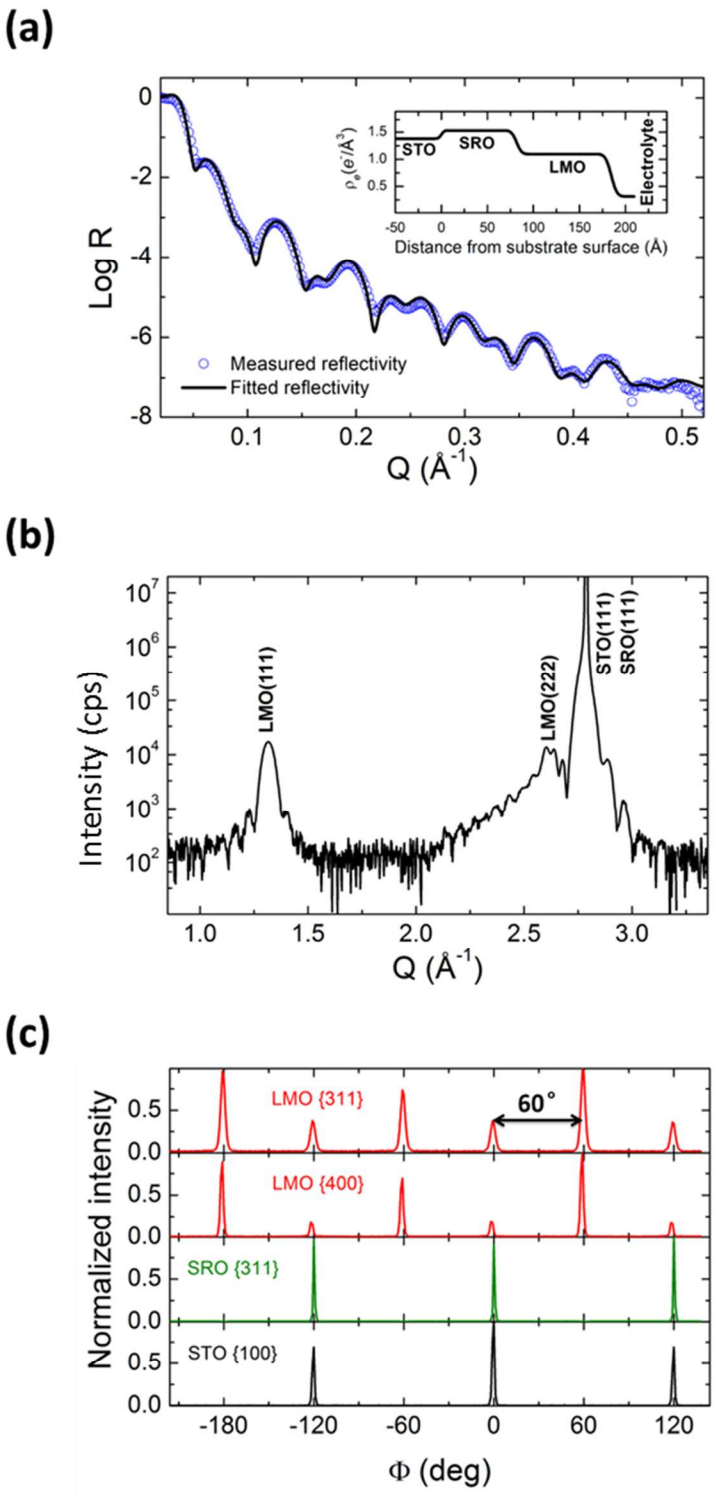

Figure 2: X-ray scattering characterization of as-deposited film. (a) X-ray reflectivity data (blue circles) and model best fit (black line). Inset shows electron density profile model for best fit; (b) specular X-ray crystal truncation rod data; (c) off-specular phi-scan of substrate $SrTiO_3$ Bragg peak family {100} (black), buffer layer $SrRuO_3$ Bragg peak family {311} (green) and $LiMn_2O_4$ Bragg peak family {400} {311} (red).

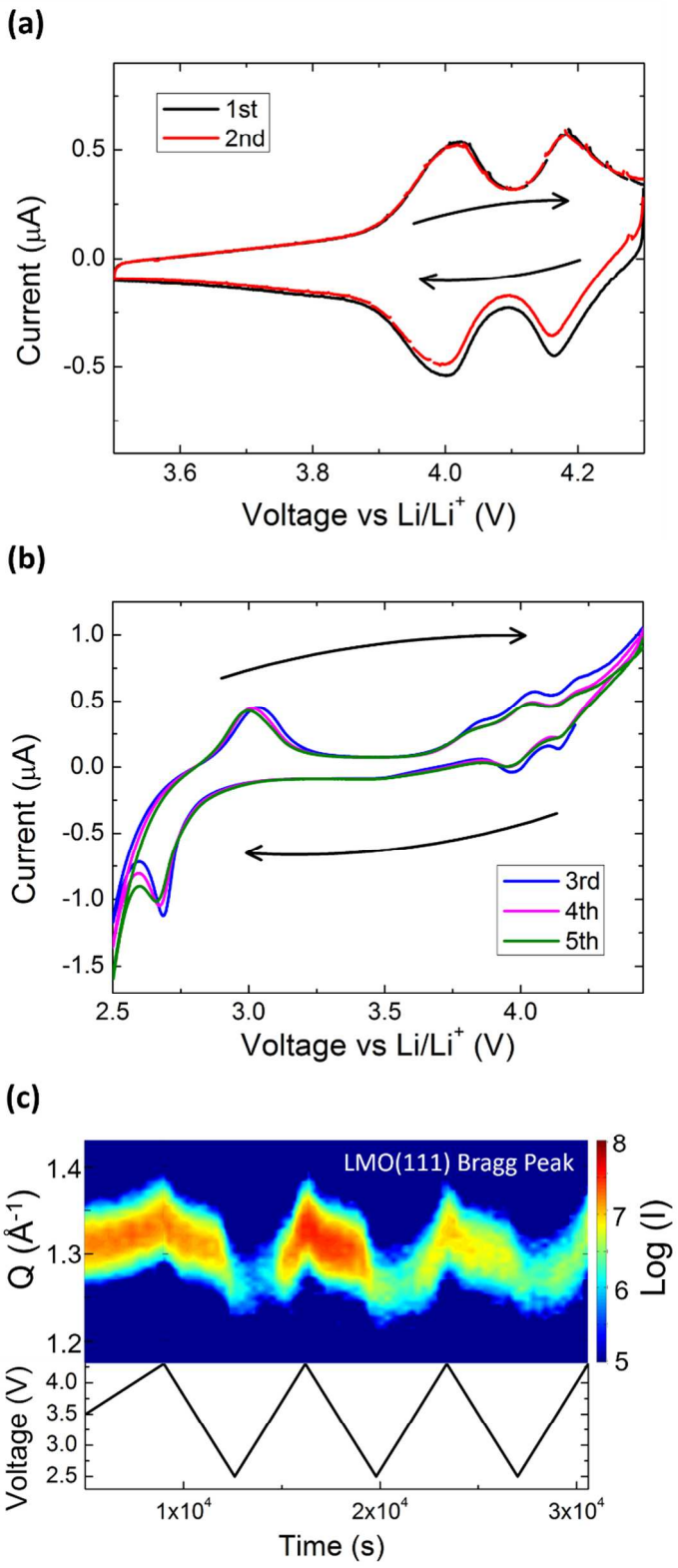

Figure 3: (a) CV curve for first 2 cycles between 3.5 V and 4.3 V; (b) CV curve for 3rd to 5th cycles between 2.5 V and 4.3V; (c) 2D color map of LMO (111) Bragg peak changes with the related voltage.

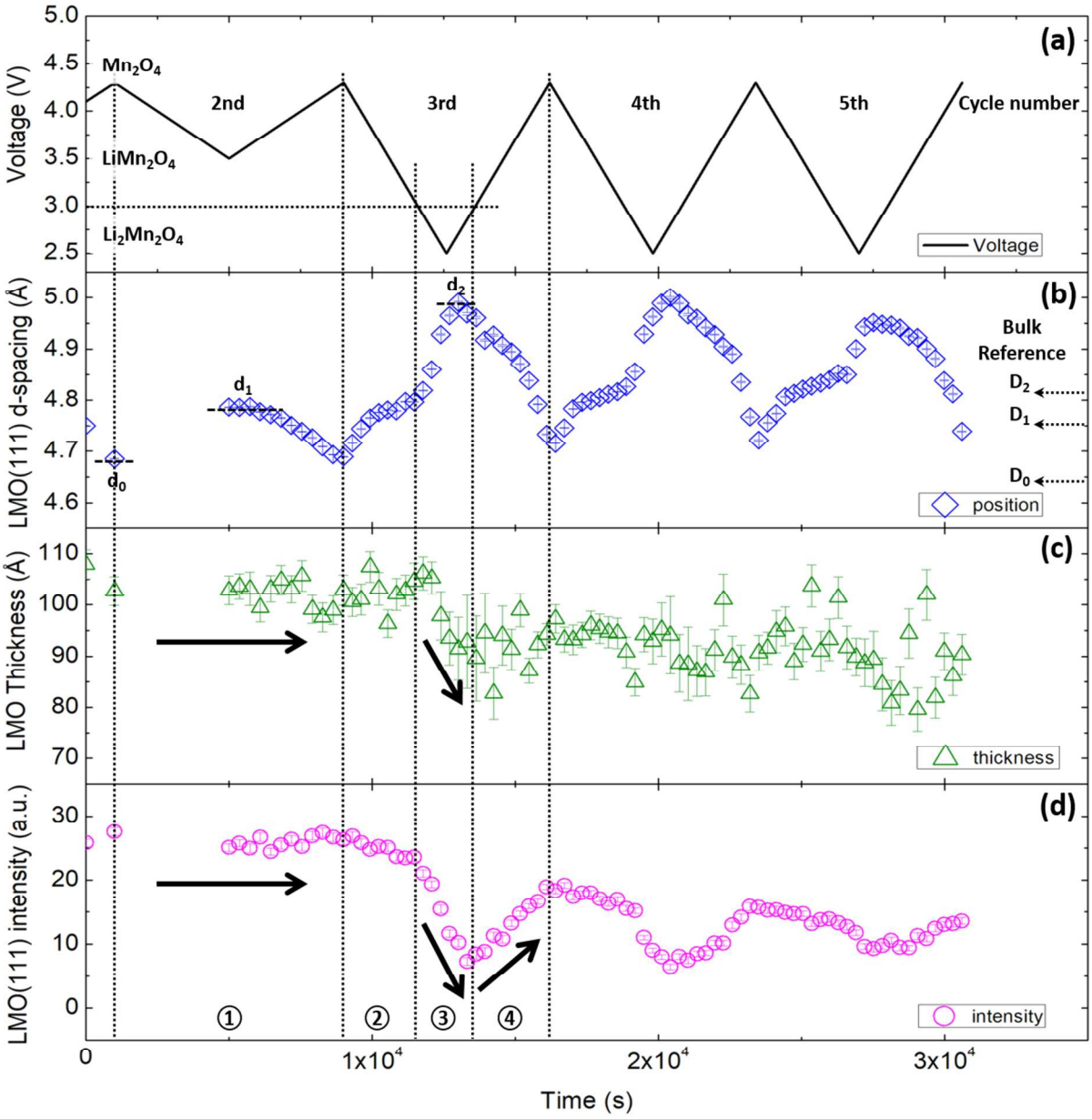

Figure 4: The time sequence of the $Li_xMn_2O_4$ ($0 \leq x \leq 2$) thin film parameters with associated voltage. (a) voltage profile; (b) d-spacing of LMO (111) Bragg peak. D_0, D_1 and D_2 marks the d-spacing of bulk λ-Mn_2O_4, $LiMn_2O_4$ and $Li_2Mn_2O_4$ respectively. d_0, d_1 and d_2 marks the measured d-spacing of LMO film at those 3 states; (c) LMO film thickness; (d) integrated intensity of LMO (111) Bragg peak. Vertical dash lines divide 2nd cycle into region ① and 3rd cycle into region ②③④.

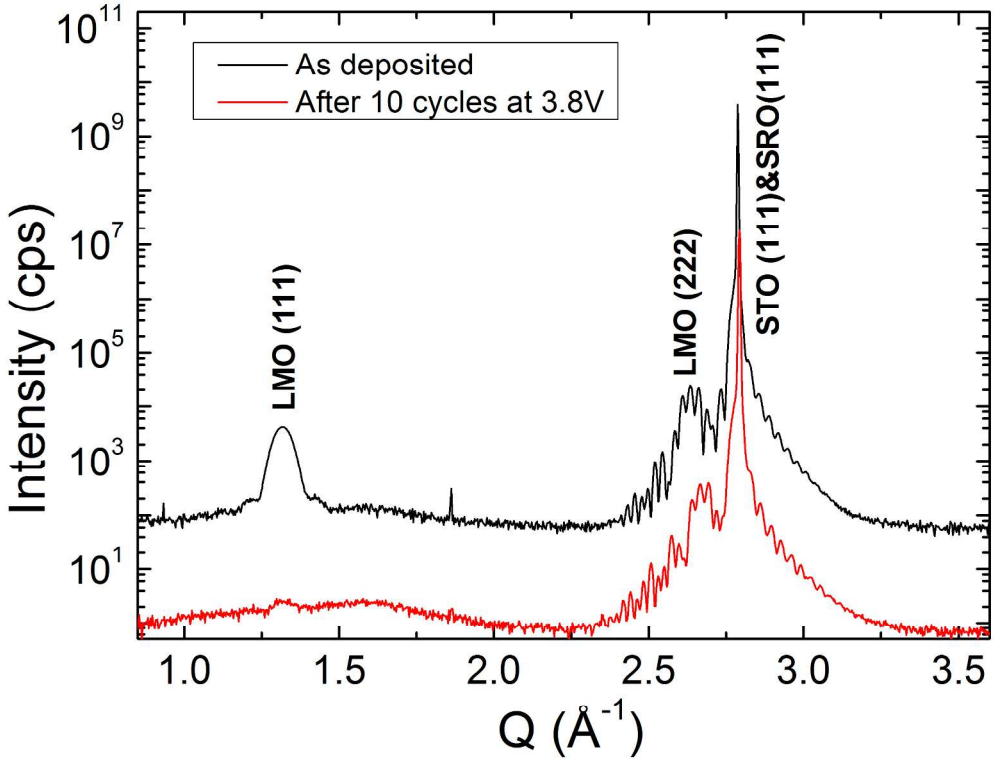

Figure 5: Full range specular CTR scans for a 10 nm LMO / 30 nm SRO / STO (111) thin film sample at as-deposited state and after 10 cycles.

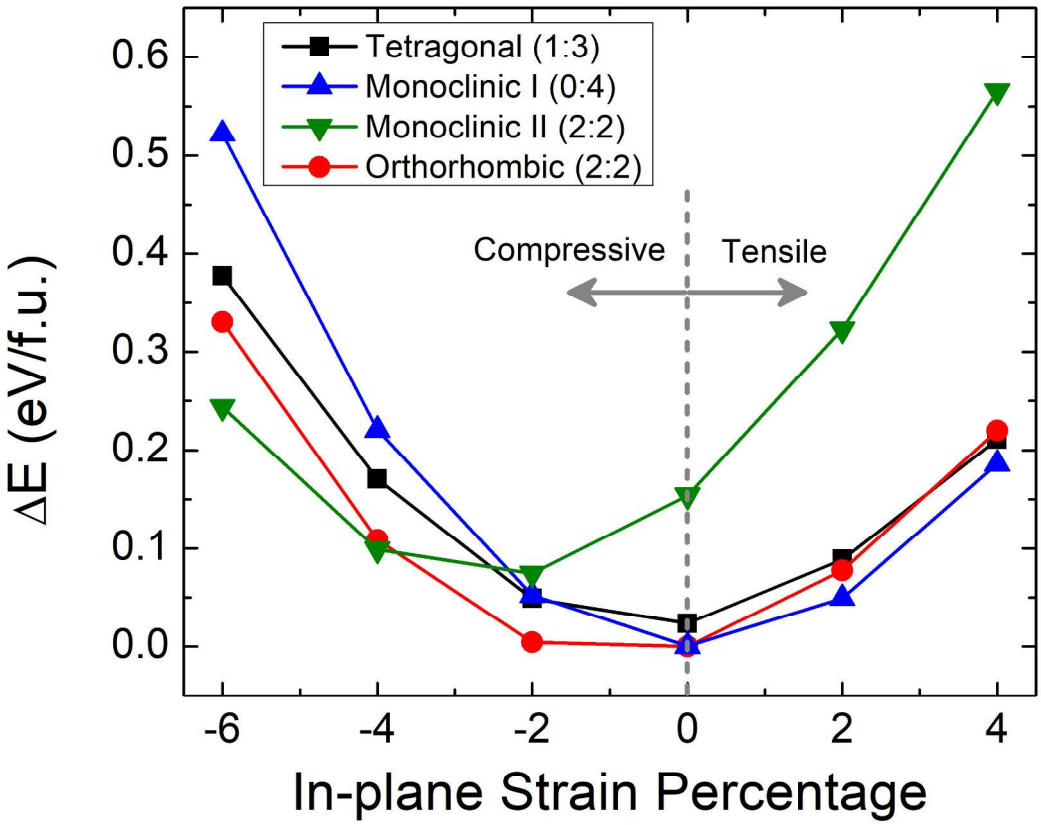

Figure 6: DFT results for relative energy per formula unit *vs* in-plane strain percentage for various LMO phases (see Figure 1) that differ solely by their Mn-site distributions. The vertical grey dash line splits the in-plane strain into compressive and tensile regimes.

Cited References:

(1) Banerjee, J.; Dutta, K., Materials for Electrodes of Li-Ion Batteries: Issues Related to Stress Development. *Crit Rev Solid State* **2017,** *42* (3), 218-238.

(2) Nitta, N.; Wu, F. X.; Lee, J. T.; Yushin, G., Li-ion battery materials: present and future. *Mater Today* **2015,** *18* (5), 252-264.

(3) Deng, D., Li-ion batteries: basics, progress, and challenges. *Energy Sci Eng* **2015,** *3* (5), 385-418.

(4) Chen, J. J., Recent Progress in Advanced Materials for Lithium Ion Batteries. *Materials* **2013,** *6* (1), 156-183.

(5) Goodenough, J. B.; Kim, Y., Challenges for Rechargeable Li Batteries. *Chem Mater* **2010,** *22* (3), 587-603.

(6) Thackeray, M. M.; David, W. I. F.; Bruce, P. G.; Goodenough, J. B., Lithium Insertion into Manganese Spinels. *Mater Res Bull* **1983,** *18* (4), 461-472.

(7) Xia, Y.; Sakai, T.; Fujieda, T.; Yang, X.; Sun, X.; Ma, Z.; McBreen, J.; Yoshio, M., Correlating Capacity Fading and Structural Changes in Li1+ y Mn2− y O 4− δ Spinel Cathode Materials: A Systematic Study on the Effects of Li/Mn Ratio and Oxygen Deficiency. *Journal of The Electrochemical Society* **2001,** *148* (7), A723-A729.

(8) Yunjian, L.; Xinhai, L.; Huajun, G.; Zhixing, W.; Qiyang, H.; Wenjie, P.; Yong, Y., Electrochemical performance and capacity fading reason of LiMn 2 O 4/graphite batteries stored at room temperature. *Journal of Power Sources* **2009,** *189* (1), 721-725.

(9) Arora, P.; White, R. E.; Doyle, M., Capacity fade mechanisms and side reactions in lithium ion batteries. *Journal of the Electrochemical Society* **1998,** *145* (10), 3647-3667.

(10) Lu, C.-H.; Lin, S.-W., Dissolution kinetics of spinel lithium manganate and its relation to capacity fading in lithium ion batteries. *Journal of materials research* **2002,** *17* (6), 1476-1481.

(11) Warburton, R. E.; Iddir, H.; Curtiss, L. A.; Greeley, J., Thermodynamic Stability of Low- and High-Index Spinel LiMn2O4 Surface Terminations. *Acs Appl Mater Inter* **2016,** *8* (17), 11108-11121.

(12) Zhao, L.; Che´nard, E.; Capraz, O. O.; Sottos, N. R.; R.White, S., Direct Detection of Manganese Ions in Organic Electrolyte by UV-vis Spectroscopy. *Journal of The Electrochemical Society* **2018,** *165* (2), A345-a348.

(13) Mosbah, A.; Verbaere, A.; Tournoux, M., Phases LixMnO2λ rattachees au type spinelle. *Mater Res Bull* **1983,** *18* (11), 1375-1381.

(14) Yamada, A.; Tanaka, M., Jahn-Teller structural phase transition around 280K in LiMn 2 O 4. *Mater Res Bull* **1995,** *30* (6), 715-721.

(15) Armstrong, A. R.; Bruce, P. G., Synthesis of layered LiMnO2 as an electrode for rechargeable lithium batteries. *Nature* **1996,** *381* (6582), 499.

(16) Johnston, W.; Heikes, R., A Study of the LixMn (1-x) O System1. *Journal of the American Chemical Society* **1956,** *78* (14), 3255-3260.

(17) Hoppe, R.; Brachtel, G.; Jansen, M., Zur Kenntnis der Oxomanganate (III):, Über LiMnO2 und β - NaMnO2 [1]. *Zeitschrift für anorganische und allgemeine Chemie* **1975,** *417* (1), 1-10.

(18) Wei, Y.; Ehrenberg, H.; Bramnik, N. N.; Nikolowski, K.; Baehtz, C.; Fuess, H., In situ synchrotron diffraction study of high temperature prepared orthorhombic LiMnO 2. *Solid State Ionics* **2007,** *178* (3), 253-257.

(19) Uysal, A.; Zhou, H.; Feng, G.; Lee, S. S.; Li, S.; Cummings, P. T.; Fulvio, P. F.; Dai, S.; McDonough, J. K.; Gogotsi, Y.; Fenter, P., Interfacial ionic 'liquids': connecting static and dynamic structures. *Journal of Physics-Condensed Matter* **2015,** *27* (3).

(20) Fenter, P.; Lee, S. S., *Hydration Layer Structure at Solid/Water Interfaces*. Materials Research Society: 2014.

(21) Fenter, P.; Sturchio, N. C., Mineral-water interface structures revealed by synchrotron x-ray scattering. *Progress in Surface Science* **2004,** *77*, 171-258.

(22) Hirayama, M.; Sonoyama, N.; Ito, M.; Minoura, M.; Mori, D.; Yamada, A.; Tamura, K.; Mizuki, J.; Kanno, R., Characterization of electrode/electrolyte interface with X-ray reflectometry and epitaxial-film LiMn2O4 electrode. *Journal of the Electrochemical Society* **2007,** *154* (11), A1065-A1072.

(23) Hirayama, M.; Ido, H.; Kim, K.; Cho, W.; Tamura, K.; Mizuki, J.; Kanno, R., Dynamic Structural Changes at LiMn2O4/Electrolyte Interface during Lithium Battery Reaction. *Journal of the American Chemical Society* **2010,** *132* (43), 15268-15276.

(24) Jiang, J.; Pan, X.; Chen, C., Microstructure of epitaxial SrRuO 3 thin films on (001) SrTiO 3. *Applied physics letters* **1998,** *72* (8), 909-911.

(25) Sonoyama, N.; Iwase, K.; Takatsuka, H.; Matsumura, T.; Imanishi, N.; Takeda, Y.; Kanno, R., Electrochemistry of LiMn2O4 epitaxial films deposited on various single crystal substrates. *Journal of Power Sources* **2009,** *189* (1), 561-565.

(26) Fister, T. T.; Esbenshade, J.; Chen, X.; Long, B. R.; Shi, B.; Schleputz, C. M.; Gewirth, A. A.; Bedzyk, M. J.; Fenter, P., Lithium Intercalation Behavior in Multilayer Silicon Electrodes. *Adv Energy Mater* **2014,** *4* (7).

(27) Fister, T. T.; Long, B. R.; Gewirth, A. A.; Shi, B.; Assoufid, L.; Lee, S. S.; Fenter, P., Real-Time Observations of Interfacial Lithiation in a Metal Silicide Thin Film. *J. Phys Chem C* **2012,** *116* (42), 22341-22345.

(28) Chen, X.; Fister, T. T.; Esbenshade, J.; Shi, B.; Hu, X. Y.; Wu, J. S.; Gewirth, A. A.; Bedzyk, M. J.; Fenter, P., Reversible Li-Ion Conversion Reaction for a TixGe Alloy in a Ti/Ge Multilayer. *Acs Appl Mater Inter* **2017,** *9* (9), 8169-8176.

(29) Giannozzi, P.; Baroni, S.; Bonini, N.; Calandra, M.; Car, R.; Cavazzoni, C.; Ceresoli, D.; Chiarotti, G. L.; Cococcioni, M.; Dabo, I., QUANTUM ESPRESSO: a modular and open-source software project for quantum simulations of materials. *Journal of physics: Condensed matter* **2009,** *21* (39), 395502.

(30) Hamann, D., Optimized norm-conserving Vanderbilt pseudopotentials. *Physical Review B* **2013,** *88* (8), 085117.

(31) Schlipf, M.; Gygi, F., Optimization algorithm for the generation of ONCV pseudopotentials. *Computer Physics Communications* **2015,** *196*, 36-44.

(32) Cococcioni, M.; de Gironcoli, S., Linear response approach to the calculation of the effective interaction parameters in the $\mathrm{LDA}+\mathrm{U}$ method. *Physical Review B* **2005,** *71* (3), 035105.

(33) Chevrier, V. L.; Ong, S. P.; Armiento, R.; Chan, M. K. Y.; Ceder, G., Hybrid density functional calculations of redox potentials and formation energies of transition metal compounds. *Physical Review B* **2010,** *82* (7), 075122.

(34) Zhou, F.; Cococcioni, M.; Marianetti, C. A.; Morgan, D.; Ceder, G., First-principles prediction of redox potentials in transition-metal compounds with $\mathrm{LDA}+U$. *Physical Review B* **2004,** *70* (23), 235121.

(35) Liu, W.-W.; Wang, D.; Wang, Z.; Deng, J.; Lau, W.-M.; Zhang, Y., Influence of magnetic ordering and Jahn-Teller distortion on the lithiation process of LiMn2O4. *Physical Chemistry Chemical Physics* **2017,** *19* (9), 6481-6486.

(36) Singh, D. J., Magnetic and electronic properties of ${\mathrm{LiMnO}}_{2}$s. *Physical Review B* **1997,** *55* (1), 309-312.

(37) Greedan, J. E.; Raju, N. P.; Davidson, I. J., Long Range and Short Range Magnetic Order in Orthorhombic LiMnO2. *Journal of Solid State Chemistry* **1997,** *128* (2), 209-214.

(38) Feng, L.; Chang, Y.; Wu, L.; Lu, T., Electrochemical behaviour of spinel LiMn2O4 as positive electrode in rechargeable lithium cells. *Journal of power sources* **1996,** *63* (1), 149-152.

(39) Urban, A.; Lee, J.; Ceder, G., The Configurational Space of Rocksalt-Type Oxides for High-Capacity Lithium Battery Electrodes. *Adv Energy Mater* **2014,** *4* (13).

(40) Depicciotto, L. A.; Thackeray, M. M., Transformation of Delithiated Livo2 to the Spinel Structure. *Mater Res Bull* **1985,** *20* (2), 187-195.

(41) Shao-Horn, Y.; Hackney, S. A.; Kahaian, A. J.; Kepler, K. D.; Skinner, E.; Vaughey, J. T.; Thackeray, M. M., Structural fatigue in spinel electrodes in Li/Li-x[Mn-2]O-4 cells. *Journal of Power Sources* **1999,** *81*, 496-499.

(42) Didier, C.; Guignard, M.; Denage, C.; Szajwaj, O.; Ito, S.; Saadoune, I.; Darriet, J.; Delmas, C., Electrochemical Na-Deintercalation from NaVO2. *Electrochem Solid St* **2011,** *14* (5), A75-A78.

(43) Mishra, S. K.; Ceder, G., Structural stability of lithium manganese oxides. *Physical Review B* **1999,** *59* (9), 6120-6130.

(44) Vetter, J.; Novák, P.; Wagner, M. R.; Veit, C.; Möller, K. C.; Besenhard, J. O.; Winter, M.; Wohlfahrt-Mehrens, M.; Vogler, C.; Hammouche, A., Ageing mechanisms in lithium-ion batteries. *Journal of Power Sources* **2005,** *147* (1), 269-281.

(45) Lin, C.; Tang, A.; Mu, H.; Wang, W.; Wang, C., Aging mechanisms of electrode materials in lithium-ion batteries for electric vehicles. *Journal of Chemistry* **2015,** *2015*.

(46) Çapraz, Ö. Ö.; Bassett, K. L.; Gewirth, A. A.; Sottos, N. R., Electrochemical Stiffness Changes in Lithium Manganese Oxide Electrodes. *Adv Energy Mater* **2017,** *7* (7).

(47) Ulvestad, A.; Cho, H. M.; Harder, R.; Kim, J. W.; Dietze, S. H.; Fohtung, E.; Meng, Y. S.; Shpyrko, O. G., Nanoscale strain mapping in battery nanostructures. *Applied Physics Letters* **2014,** *104* (7).

(48) Ulvestad, A.; Singer, A.; Cho, H. M.; Clark, J. N.; Harder, R.; Maser, J.; Meng, Y. S.; Shpyrko, O. G., Single Particle Nanomechanics in Operando Batteries via Lensless Strain Mapping. *Nano Letters* **2014,** *14* (9), 5123-5127.

(49) Chung, K. Y.; Kim, K. B., Investigations into capacity fading as a result of a Jahn-Teller distortion in 4 V LiMn2O4 thin film electrodes. *Electrochim Acta* **2004,** *49* (20), 3327-3337.

(50) Gummow, R. J.; Dekock, A.; Thackeray, M. M., Improved Capacity Retention in Rechargeable 4v Lithium Lithium Manganese Oxide (Spinel) Cells. *Solid State Ionics* **1994,** *69* (1), 59-67.

(51) Reed, J.; Ceder, G.; Van der Ven, A., Layered-to-spinel phase transition in LixMnO2. *Electrochem Solid St* **2001,** *4* (6), A78-A81.

(52) Chen, K. S.; Xu, R.; Luu, N. S.; Secor, E. B.; Hamamoto, K.; Li, Q. Q.; Kim, S.; Sangwan, V. K.; Balla, I.; Guiney, L. M.; Seo, J. W. T.; Yu, X. K.; Liu, W. W.; Wu, J. S.; Wolverton, C.; Dravid, V. P.; Barnett, S. A.; Lu, J.; Amine, K.; Hersam, M. C., Comprehensive Enhancement of Nanostructured Lithium-Ion Battery Cathode Materials via Conformal Graphene Dispersion. *Nano Lett* **2017,** *17* (4), 2539-2546.

(53) Mohanty, D.; Li, J. L.; Abraham, D. P.; Huq, A.; Payzant, E. A.; Wood, D. L.; Daniel, C., Unraveling the Voltage-Fade Mechanism in High-Energy-Density Lithium-Ion Batteries: Origin of the Tetrahedral Cations for Spinel Conversion. *Chem Mater* **2014,** *26* (21), 6272-6280.

Table of Contents Graphic: